PLASMA DYNAMICS

XXI. PLASMA PHYSICS*

Academic and Research Staff

Prof. G. Bekefi
Prof. W. P. Allis
Prof. S. C. Brown
Prof. J. C. Ingraham
Prof. B. L. Wright
Dr. W. M. Manheimer
J. J. McCarthy
W. J. Mulligan

Graduate Students

M. L. Andrews
R. L. Becker
A. J. Cohen
D. L. Flannery
R. L. Kronquist
P. Mix
L. D. Pleasance
G. L. Rogoff
J. K. Silk
E. N. Spithas
D. W. Swain
J. H. Vellenga
D. L. Workman

RESEARCH OBJECTIVES

The plasma physics group continues to study the interactions between electromagnetic oscillations and ionized gases. These studies are made over a very wide spectrum of frequencies ranging from tens of kilocycles per second through microwaves and infrared frequencies to the optical. The low frequencies bring out the characteristics of the ion motions whereas the high-frequency regime aims at investigating the electron interactions. In the experiments we use the standard radio and microwave techniques together with the more novel laser methods.

In earlier years we have concentrated on those aspects of wave-plasma interactions in which the waves cause but a small pertubation of the medium. Now our interest tend more and more towards nonlinear phenomena as, for example, coupling between particles and waves, parametric coupling of waves with waves and turbulent plasma phenomena.

The experimental and theoretical studies carried out in the group are closely interwoven. Theoretical investigations are being made regarding the propagation of large amplitude waves in an ionized gas, electromagnetic emission from plasma oscillation in a highly turbulent gas and stochastic acceleration of charged particles. Particular attention is being paid to such problems as particle trapping in the potential well of a longitudinal oscillation, wave-wave coupling and parametric growth of oscillations.

G. Bekefi

A. EXACT NONLINEAR UNDAMPED WAVES IN A COLLISIONLESS PLASMA†

1. Moving Frame

Exact solutions of the collisionless Boltzmann and Poisson equations are easy to find by a method for studying interacting electron beams, which was introduced by Sen[1] and further discussed by Bernstein, Greene and Kruskal.[2] If there is a frame moving with velocity u in which the potential is static $V = V(x-ut)$, any distribution that is a function only of the constants of motion of the electrons and ions will satisfy the Boltzmann equation, and Poisson's equation is solved by quadratures.

*This work was supported principally by the U.S. Atomic Energy Commission (Contract AT(30-1)-1842).

†This work was done partly at The Los Alamos Scientific Laboratory under U.S. Atomic Energy Commission Contract W-7405-Eng-36 with the University of California.

Let us chose electron variables scaled to thermal energies and write

$$v^2 \text{ for } mv_x^2/2kT$$

$$x^2 \text{ for } m(x-ut)^2/2kT \tag{1}$$

$$\phi \text{ for } e(V+V_o)\ kT \geq 0.$$

In the moving frame (Fig. XXI-1)

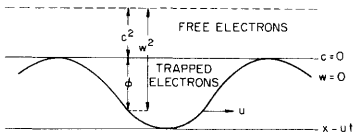

Fig. XXI-1. Potential and kinetic energy diagram.

$$w = v - u$$

$$c^2 = w^2 - \phi, \tag{2}$$

where c^2 is the energy constant, and we define the velocity $c = \sqrt{w^2 - \phi}$ to have the same sign as w.

2. Distribution in Velocity

Any function of the variables v_y, v_z, u, c will satisfy the collisionless Boltzmann equation. We wish, however, to represent waves in a plasma of stationary ions and in which the electrons have a Maxwell distribution in the absence of a potential (ϕ=0). Such a distribution function is

$$f_f = \frac{n_o}{\sqrt{\pi}} e^{-(u+c)^2}. \tag{3}$$

This function is not the only one satisfying the required conditions, but if it is linearized by expanding in powers of ϕ, it yields exactly the function of linear theory:

$$f = \left(1 + \frac{\phi/2}{u-v}\frac{\partial}{\partial v}\right)\frac{n_o}{\sqrt{\pi}} e^{-v^2}. \tag{4}$$

All of the results of linear theory are therefore contained in the assumed function (3).

The choice of the arbitrary constant V_o in the potential ϕ such that $\phi_{min} = 0$ is

equivalent to chosing a Maxwellian distribution at the coordinate marked f_M in Fig. XXI-2, and makes c^2 negative for electrons trapped in the potential wells. The

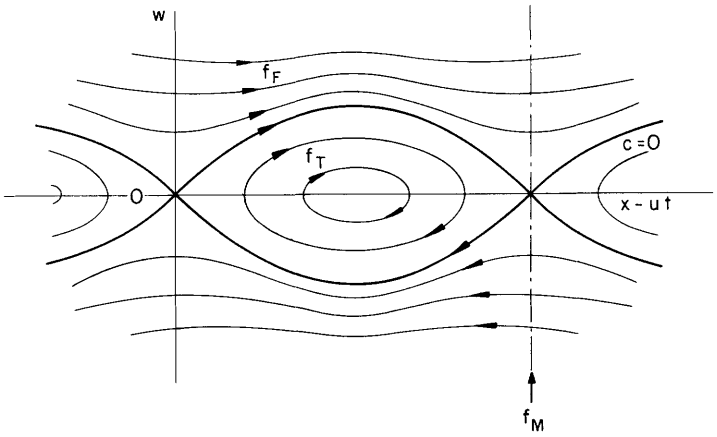

Fig. XXI-2. Trajectories in phase space.

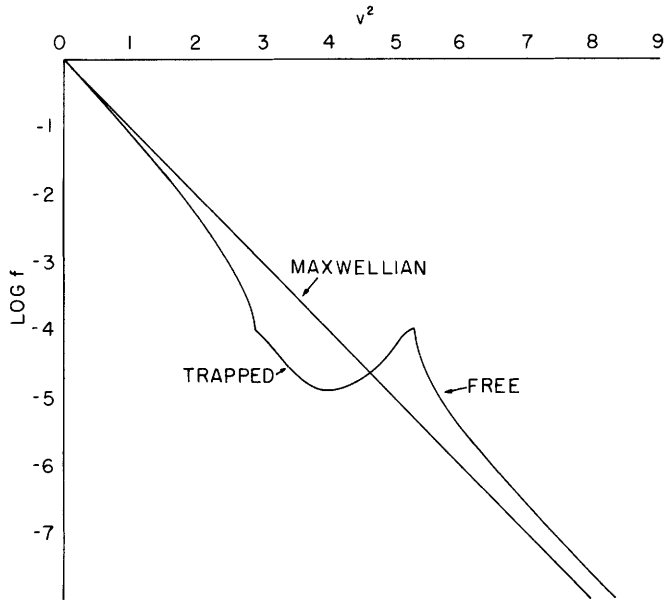

Fig. XXI-3. Logarithm of the assumed distribution in velocity.

distribution (3) is therefore complex for trapped electrons. We shall take only the real part of it

$$f_t = \frac{n_o}{\pi} e^{-u^2-c^2} \cosh 2 u c; \qquad (5)$$

that is we drop the odd powers of c because they change sign (are not constants of the motion) when electrons are reflected from the walls of the potential wells. This means that for any level above the potential well in Fig. XXI-1 there will be unequal numbers of electrons going to the right and to the left, but in the potential wells these numbers are equal. This is necessary if we are to have a stationary state. Any lack of summetry in the potential wells will lead to a sloshing of the trapped electrons back and forth in the well with eventual symmetrization by phase mixing. This has been studied by O'Neil.[3] We are studying the steady-state waves that propagate after phase mixing has taken place. The distribution defined by (3) and (5) is continuous everywhere but has a discontinuous first derivative at the top of the well (Fig. XXI-3). This is allowed in a collisionless plasma. The distribution (3) and (5) is probably the only one satisfying the four conditions:

A Static in a moving frame

B Satisfies the linear limit

C Everywhere continuous

D Analytic in c^2.

3. Electron Density

We may now integrate (3) and (5) over all velocities to obtain the electron density

$$n_- = \frac{n_o}{2} \sum_0^\infty K_a(-\phi)^a = n_o\left[1 - \frac{\mathcal{H}'}{2}\right], \tag{6}$$

where the coefficients K_a are confluent hypergeometric functions

$$M(a,1/2,-u^2) = (-1)^a \frac{a!}{2} K_a \tag{7}$$

with the signs chosen so that they are all positive for large u.

$$K_o = 2 \qquad K_1 = \text{Real } Z'(u)$$

$$a(a+1)\, K_{a+1} = (u^2-2a+1/2)K_a - (1-1/2a)K_{a-1}. \tag{8}$$

Here Z(u) is the plasma dispersion function as defined and tabulated by Fried and Conte.[4] The functions u^2K_1 and $-2u^2K_2$ are shown in Fig. XXI-4. There are two interesting limits to the sum (6):

$$n_- \to n_o(1-2u^2\phi)\, e^\phi, \qquad \text{as } u^2 \to 0 \tag{9}$$

$$n_- \to \frac{n_o}{\sqrt{1+\phi/u^2}}, \qquad \text{as } T \to 0. \tag{10}$$

For $u^2 = 0$, the electrons have a Boltzmann distribution in the potential with a maximum density over the center of the wells, $\phi = \phi_{max}$. A finite-phase velocity reduces

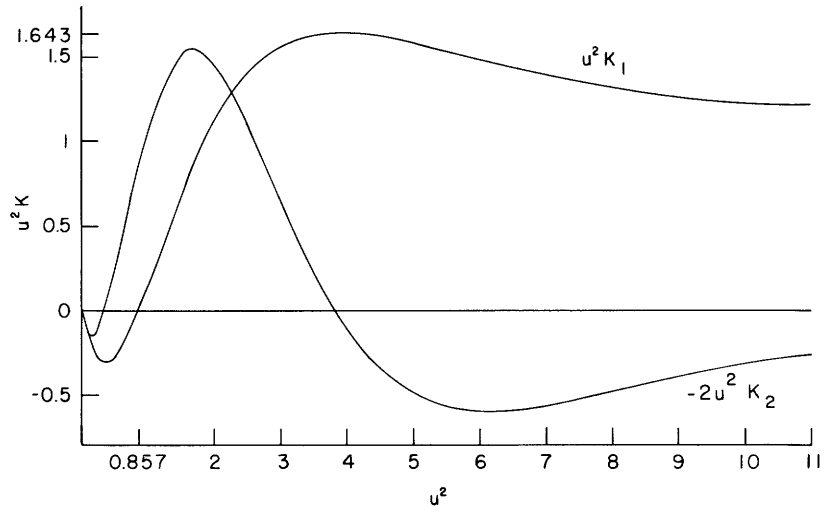

Fig. XXI-4. Plasma functions u^2K_1 and $-2u^2K_2$.

the density of electrons over the center of the well and eventually reduces it below the density at zero potential. This is so because the free electrons have a higher velocity, and hence lower density, at high ϕ. As we shall see, this reversal is necessary to produce positive space charge at high potentials and hence self-consistency. The function K_1 changes sign for $2u^2 = 1.715$. There are no self-consistent waves at low velocity.

4. Poisson's Equation

The number n_o is the electron density at zero potential. For phase velocities above $u = 0.926$ the average electron density is less than n_o and for average space-charge neutrality the positive ion density must also be less than n_o.

$$n_+ = n_o\left(1 - \frac{C}{2}\right). \tag{11}$$

Then

$$n_- - n_+ = n_o(C - \mathcal{K}')/2 \tag{12}$$

and

$$\frac{\partial^2\phi}{\partial x^2} = \omega_o^2(C - \mathscr{K}'), \tag{13}$$

where

$$\omega_o^2 = \frac{n_o e^2}{\epsilon_o m} = \frac{2\omega_p^2}{2 - C}. \tag{14}$$

Poisson's equation integrates once to give

$$E^2 = 2\omega_o^2\phi\,(C - \mathscr{K}), \tag{15}$$

where

$$\mathscr{K} = \sum_1^\infty \frac{-K_a}{a+1}(-\phi)^a, \tag{16}$$

and the constant of integration has been taken such that $E = 0$ at $\phi = 0$.

Let ϕ_o be the first positive zero of (15). Then provided $0 < C < 2$, E^2 will be positive in the interval $0 \leq \phi \leq \phi_o$, and there will be no net space charge between these limits, as $E = 0$ at both ends. Conversely, the potential amplitude ϕ_o can have any value below the first maximum of $\mathscr{K}(\phi) \leq 2$. Then $C = \mathscr{K}(\phi_o)$.

Equation (15) then integrates to give the phase of the wave in terms of the potential

$$\omega_o x = \int_0^\phi \frac{d\phi}{2(C - \mathscr{K})\,\phi} = \frac{\sqrt{2A}\,dy}{\sqrt{C - \mathscr{K}}}, \tag{17}$$

where $\phi = Ay^2$.

5. Cold Plasma Waves

In the cold plasma limit it is more convenient to write

$$n_+ = \frac{n_o}{1 + A}. \tag{18}$$

The integration of Poisson's equation then yields

$$\phi/u^2 = A(1 + \sin\phi)(2 + A + A\sin\theta),$$

where

$$\omega_p x/u = (1+A)\theta - A \cos \theta. \tag{19}$$

The fundamental frequency of the wave $\omega_p/(1+A)$ is reduced as the amplitude increases, but is independent of the phase velocity u which is quite arbitrary. Equation 19 introduces the first harmonic, however, and there is a phase modulation that has the effect of broadening the maxima and sharpening the minima of ϕ.

6. Small-Amplitude Waves

For small, but not very small, amplitudes

$$\mathcal{H} = \frac{1}{2}K_1\phi - \frac{1}{3}K_2\phi^2. \tag{20}$$

The integral (17) is then elliptic and yields the Jacobian elliptic function

$$\phi = A\,\mathrm{sn}^2\left(\frac{\omega x}{2u}, k^2\right), \tag{21}$$

where k^2, the modulus of the elliptic function, is given by

$$k^2 = \frac{2AK_2}{3K_1 - 2AK_2}$$

$$\omega^2 = \omega_o^2 u^2 \left(K_1 - \frac{2}{3}AK_2\right) \tag{22}$$

$$\omega_p^2 = \omega_o^2 \left(1 - A\frac{K_1 - \frac{2}{3}AK_2}{4}\right).$$

Clearly, K_1 must be positive ($u^2 > 1.715$), and there is a maximum amplitude

$$A = \frac{3K_1}{4K_2} \tag{23}$$

for which the elliptic function becomes a hyperbolic tangent. For this amplitude, however, the approximation (20) is no longer valid, and it is unknown whether the full series (16) leads to an upper limit. For low amplitudes the elliptic function approaches a sine function, and the dispersion

$$\omega = \omega_o u \sqrt{K_1} \tag{24}$$

is the same as that obtained from linear theory, except that the imaginary part of the plasma dispersion function, Z', is omitted. Hence there is no damping. The

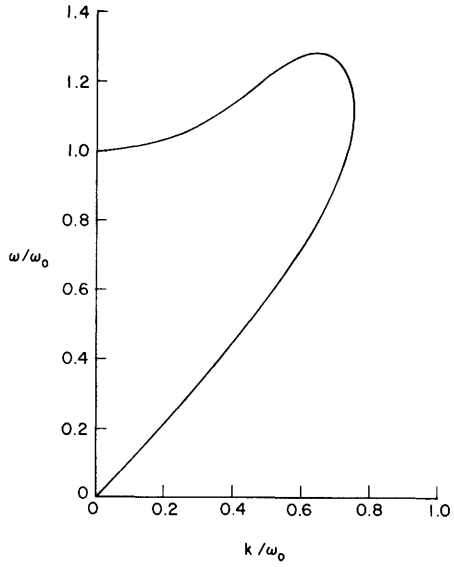

Fig. XXI-5. Dispersion relation for undamped waves.

dispersion obtained from (24) is shown in Fig. XXI-5. It has also been shown by Vlasov.[5]

7. Landau Damping

The Landau pole exists in the linearized form (4) of the distribution (3). But Landau damping is absent from the dispersion (24). Where has it been lost? Fortunately it is easy to trace. Landau damping does not come directly from (4). This function must first be analytically continued into the complex plane and then an integration performed around the pole. We also perform an analytic continuation into the potential wells, but in (5) we have only retained half of the result. The discarded part is

$$f_{t_i} = \frac{n_o}{\sqrt{\pi}} e^{-u^2-c^2} \, i \sin 2u|c|, \tag{25}$$

and integrating this between the limits $w = \pm\phi$ yields

$$n_{-1} = n_o i \sqrt{\pi} u\phi \, e^{-u^2} \tag{26}$$

plus higher powers of ϕ. This is precisely the imaginary part needed to give

$$K_1 = Z'(u)_{complex}. \tag{27}$$

The imaginary electrons represented by (25) have no place in a theory with real variables, but this calculation is sufficient to show on the one hand that damping comes from nonsymmetrical distributions of trapped electrons, and on the other hand that the integration around the Landau pole is in reality dipping into the potential wells.[6]

8. Summary

We have found a distribution function that satisfies the Vlasov equations exactly and goes to the linear limit, but without damping, for small-amplitude waves, and we can retrieve the exact Landau damping term by considering a nonsymmetrical distribution of trapped electrons. Our distribution has no poles, but the trapped distribution has negative portions for $4u^2c^2 < -\pi^2/4$. Distributions are being considered which correct this defect without altering the linear limit.

W. P. Allis

References

1. H. K. Sen, "Nonlinear Theory of Space-Charge Waves in Moving, Interacting Electron Beams," Phys. Rev. 97, 849 (1955).
2. I. B. Bernstein, J. M. Greene, and M. D. Kruskal, "Exact Nonlinear Plasma Oscillations," Phys. Rev. 108, 546 (1957).
3. T. O'Neil, "Collisionless Damping of Nonlinear Plasma Oscillations," Phys. Fluids 8, 2255 (1965).
4. B. D. Fried and S. D. Conte, The Plasma Dispersion Function (Academic Press, Inc., New York, 1961).
5. A. A. Vlasov, Many-Particle Theory and Its Application to Plasma (Gordon and Breach, New York, 1961).
6. W. P. Allis, Electrons, Ions, and Waves (The M.I.T. Press, Cambridge, Mass., 1967), p. 269.

B. DIFFUSION WAVE EXPERIMENT

This report covers further progress on the diffusion wave experiment discussed in Quarterly Progress Report No. 87 (pages 64-71). Specifically, a more appropriate theory for the radial phase and amplitude profiles of the waves has been developed, which sucessfully explains the observed data with a minimum of adjustable parameters.

In the previous report, the experimental geometry, plasma parameters, wave excitation and detection methods, and some theoretical aspects, including the wave theory assuming Bohm-type diffusion, were discussed. Also, initial fits to data with the Bohm theory were presented, in which the radius of the plasma was divided into two regions with generally different diffusion and end-loss parameters. The fits were satisfactory, but the theory did not correctly predict the observed frequency dependence. That is, fits for two different exciting frequencies could not be obtained by changing only the frequency variable in the theory. Furthermore, end-loss rates needed for fits were lower than would be expected physically for this longitudinally free-streaming plasma. (In one case a loss rate of zero gave the best fit.) Thus a more satisfactory theory was needed.

1. Diffusion Theory

In general, at least three types of diffusion could occur in the experimental plasma, the type depending on the effect of conducting end walls and the noise level of instabilities.

A quiet plasma not suffering from end effects should diffuse at the classical ambipolar rate in the appropriate limit for the experimental plasma:

$$\vec{\Gamma}_\perp = \frac{e\nu_{-+}}{m_-\omega_-^2}\nabla_\perp n(T_+ + T_-),$$

where ν_{-+} is the electron-ion momentum transfer collision frequency; T_+, T_- are temperatures in volts; and ω_- is the electron cyclotron frequency. Here, ν_{-+} is approximately proportional to $\left(N/T_-^{3/2}\right)$. For Bohm diffusion,

$$\vec{\Gamma}_\perp = \frac{c}{B}\nabla_\perp n(T_+ + T_-),$$

where c is a constant generally unknown but often ~1/16 experimentally. Bohm diffusion is expected when the noise level exceeds some critical value, such that the Bohm rate equals the always present collisional diffusion rate.

The third possibility, free-ion diffusion, will occur if electrons are short-circuited across the magnetic field lines by conducting end walls. In this case

$$\vec{\Gamma}_\perp \geq \frac{e\nu_{+n}}{m_+\omega_+^2}\nabla_\perp (nT_+),$$

where ν_{+n} is the ion-neutral momentum transfer collision frequency. The inequality sign applies because there may be considerable ion transport proportional to higher order spatial derivatives, caused by ion-ion collisions.[1]

An effective local diffusion coefficient may be defined:

$$D \equiv \left.\frac{|\vec{\Gamma}_\perp|}{|\nabla n|}\right|_{\nabla T_+ = \nabla T_- = 0}.$$

The experimental and predicted values of $D_\perp$ given will always be the local values at the normalization radius, approximately 0.5 cm. The following values were calculated, by using the measured plasma parameters, for the two experimental conditions reported here.

Type of Diffusion	Predicted $D_\perp$ (cm^2/sec)	
B:	530 Gauss	880 Gauss
Ambipolar, Quiet	4.4×10^3	2.3×10^3
Free-Ion, Simon	1.3×10^4	8.0×10^3
Bohm	2.6×10^4	1.3×10^4

Thus in these experiments free-ion and Bohm diffusion should result in roughly the same rate, which is only 3-4 times the ambipolar rate.

2. Ambipolar Diffusion Wave Theroy

A computer program has been written to solve the diffusion wave equation in essentially the same form as outlined in the previous report, except that the ambipolar form of the diffusion coefficient was used, incorporating the density and temperature dependence of the electron-ion collision frequency. For this theory, both the steady-state plasma density and the electron-temperature radial profiles are needed as input. The measured profiles were approximated by analytic functions. The same two adjustable parameters are involved, the diffusion parameter ($\omega/D_\perp$) and the end-loss parameter (V_s/L), both defined at the data normalization radius, ~0.5 cm. The IBM 360-65 facilities of the M. I. T. Computation Center were used for the computations.

3. Comparison of Theory and Experiment

a. B = 530 Gauss

Figures XXI-6 and XXI-7 show theoretical and experimental phase and amplitude radial profiles of the diffusion waves. The experimental points were taken with a

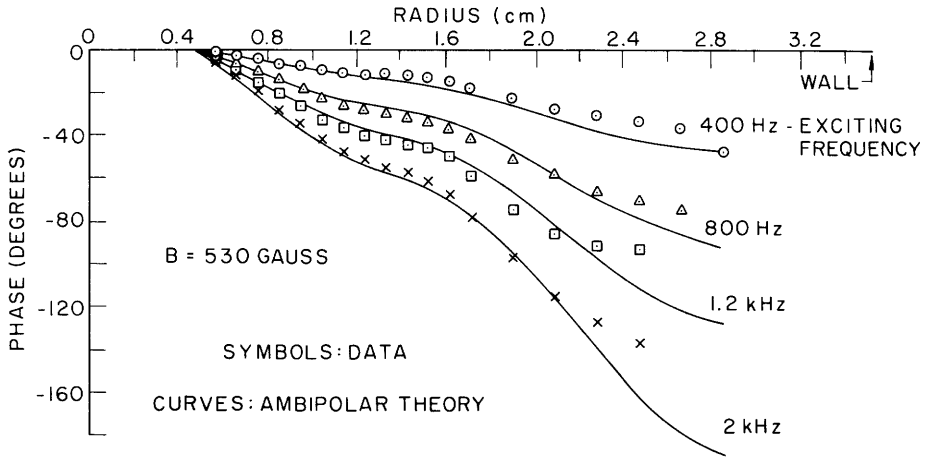

Fig. XXI-6. Experimental and theoretical diffusion wave phase profiles.

magnetic field of 530 Gauss and at lowest attainable noise levels. Figures XXI-8 and XXI-9 show the corresponding measured plasma-density and electron-temperature

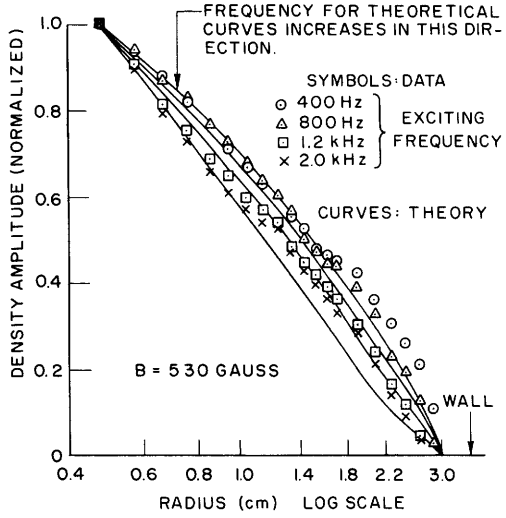

Fig. XXI-7. Experimental and theoretical diffusion-wave amplitude profiles.

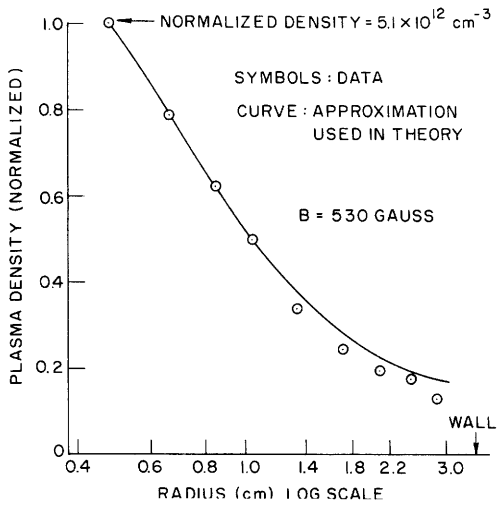

Fig. XXI-8. Plasma-density profile and approximation used in diffusion-wave theory.

profiles and the analytic approximations used in the theory. The smooth curves in Figs. XXI-1 and XXI-2 are the computer solutions from the ambipolar theory, using the values $D_{\perp} = 2.9 \times 10^3$ cm^2/sec and $V_s = 4.7 \times 10^4$ cm/sec in the adjustable parameters. The only difference between the theoretical curves is the frequency used in the diffusion parameter. The frequencies used were the four experimental values. The frequency

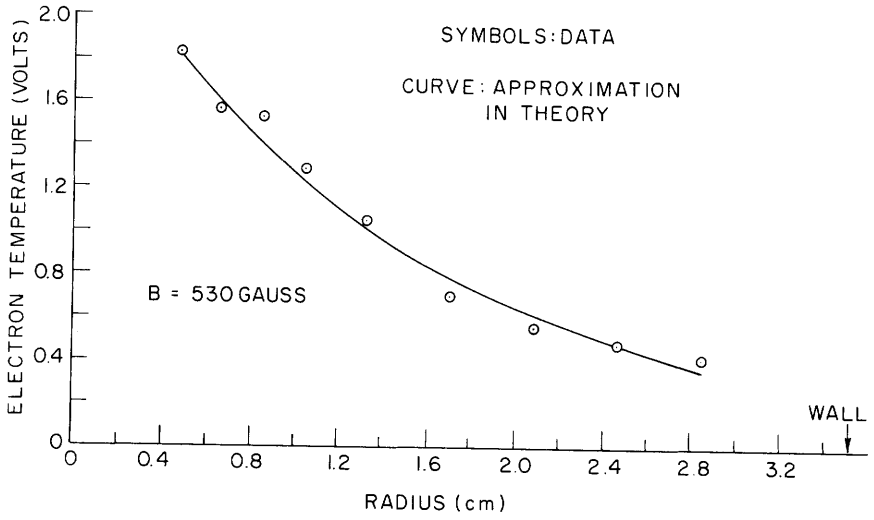

Fig. XXI-9. Electron temperature profile and approximation used in diffusion wave theory.

dependence of this theory seems satisfactory. An unexpected region of reduced phase shift per unit radius shows up in the data (Fig. XXI-1). The "bump" is centered at the radius of the anode (corrected for magnetic field curvature), and is approximately an ion Larmor radius thick. It seems logical to postulate that this is an effect attributable to the change in end conditions at the radius of the anode. The severity and position of the bump depend on the anode radius and position. Using an anode of 20% larger radius caused the bump to move out accordingly. Thus it was necessary to include in the theory a region of increased diffusion and end loss to obtain the fits in Figs. XXI-1 and XXI-2. The region is mathematically prescribed as illustrated in Fig. XXI-10. It seems significant that this phenomenological approach agrees with the frequency dependence of the data. That is, the features of the region do not have to change with frequency in order to obtain agreement with data.

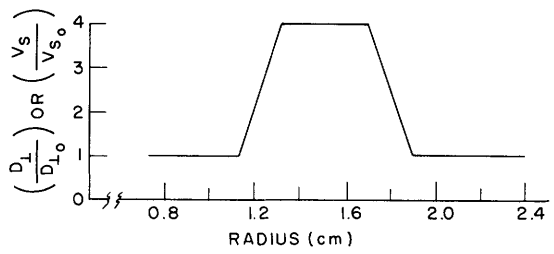

Fig. XXI-10. Region of increased diffusion and end loss inserted in theory for 530-Gauss magnetic field.

b. B = 880 Gauss

Figures XXI-11 and XXI-12 give data and theory for a stronger magnetic field. The fit procedure was the same as before, except that it was not necessary to postulate a

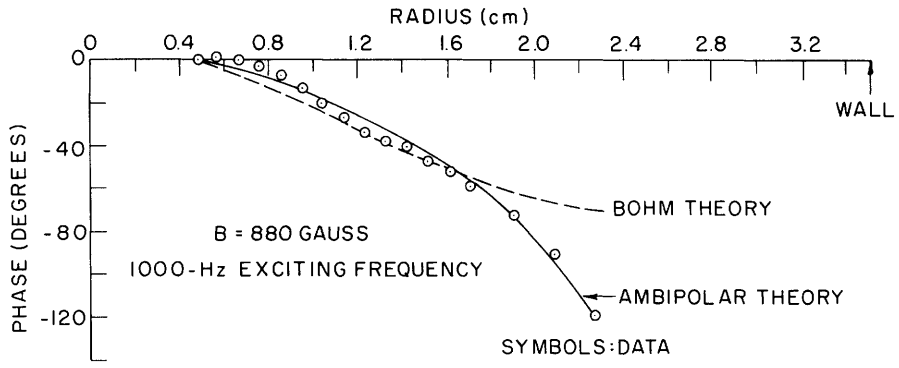

Fig. XXI-11. Experimental and two theoretical diffusion-wave phase profiles at 880-Gauss magnetic field.

region of reduced diffusion and end loss at the anode radius. Apparently the phenomenon disappeared or was not detectable at the greater magnetic field. Both types of available theory were fitted in order to gain a comparison. Identical temperature profiles were

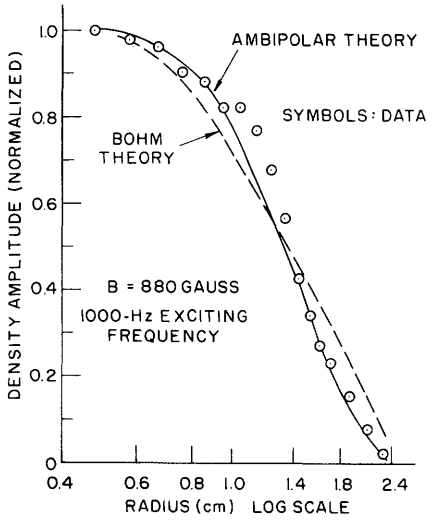

Fig. XXI-12. Experimental and two theoretical diffusion-wave amplitude profiles at 880-Gauss magnetic field.

inserted in the two theories. (The Bohm theory does not require a density profile as input.) The steady-state density and temperature profiles were fitted to data as before. The results follow.

	Predicted Value	Experimental Values	
Type of Diffusion	$D_\perp$ (cm^2/sec)	$D_\perp$ (cm^2/sec)	V_s (cm/sec)
Bohm	1.3×10^4	6.5×10^3	4.7×10^4
Ambipolar	2.3×10^3	3.9×10^3	2.2×10^5

c. Interpretation of Loss Parameter

The end-loss rate that was used as an adjustable parameter in the theory can best be viewed as an effective inverse loss time for plasma free-streaming to the end walls. A reasonable upper bound for this rate should be given by (C_s/L), where C_s is the ion acoustic velocity. Or, equivalently, the upper bound for V_s is C_s, which is about 3×10^5 cm/sec in the experiment. The values obtained for V_s all fall within the order of magnitude extending below C_s, and thus are consistent with this interpretation. A rigorous theoretical treatment of longitudinal plasma transport would be required in order to attach any greater significance to the end-loss parameter. This treatment would be difficult, if possible, and is not needed, since the present simple phenomenological approach gives satisfactory results.

d. Results of Comparisons

Three criteria seem appropriate for comparing the two theories with experiment.

(i) Correct prediction of frequency dependence.

(ii) Good agreement with data profiles at any one frequency.

(iii) Values of $D_\perp$ and V_s consistent with theoretical expectations.

The presentations of section 3a as compared with the results given in the previous report indicate that criterion (i) favors the ambipolar theory. The comparison in section 3b also favors the ambipolar theory on the basis of criterion (ii). Either theory yields a fitted value of $D_\perp$ that is consistent with its assumed diffusion mechanism, within the accuracy of the experimental and calculated values. Thus criterion (iii) favors neither theory. Over-all, the ambipolar theory gives a better explanation of the data.

4. A Check on an Important Assumption in the Theory

In the theory presented in the previous report,[2] the approximation $\partial n/\partial z = \partial T/\partial z = 0$ was made, based on the assumption that free-streaming would prevent the plasma from supporting an appreciable longitudinal pressure gradient, except at the end-wall sheaths. To check this, the longitudinal variation of the data was investigated. Figures XXI-13 and XXI-14 show probe floating potential and ion saturation current versus longitudinal position, at several different radii. Two positions are marked to show where radial profiles were taken. These profiles are shown in Figs. XXI-15, XXI-16, and XXI-17. The amplitude and phase data at the two points differed uniformly by approximately 7% and 12°, respectively. With normalization (at R = 0.47 cm) the data are practically identical. The amplitude ratio corresponds to that of the plasma

densities (Fig. XXI-17). The temperature data at the two points are identical within experimental accuracy, although the temperature appears to be slightly

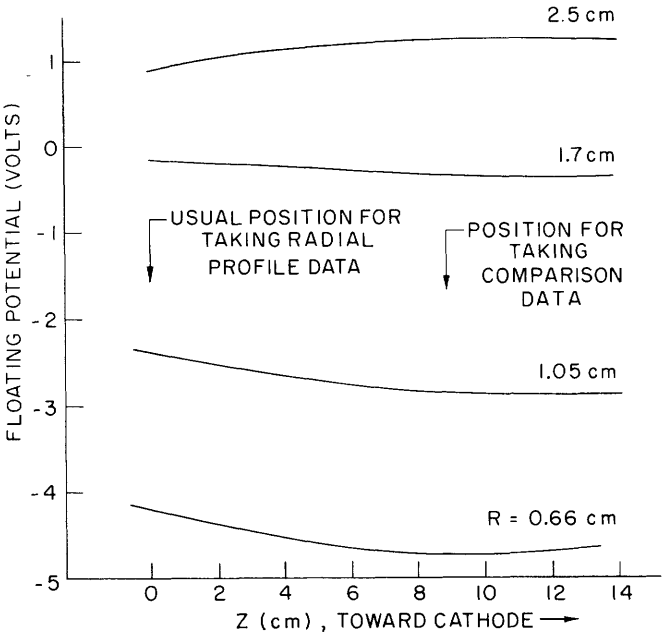

Fig. XXI-13. Probe floating potential vs longitudinal position at several radii.

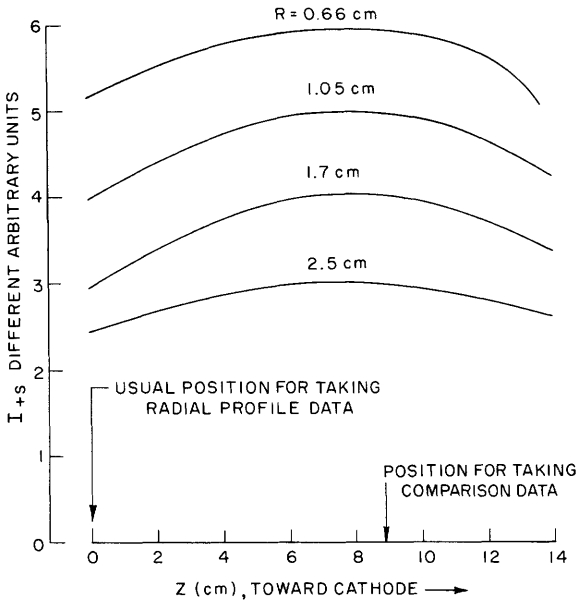

Fig. XXI-14. Probe ion saturation current vs longitudinal position at several radii.

higher nearer the cathode. The temperature profiles are almost identical to the one shown in Fig. XXI-9.

The 12° phase lag of the data farther from the cathode corresponds to a longitudinal

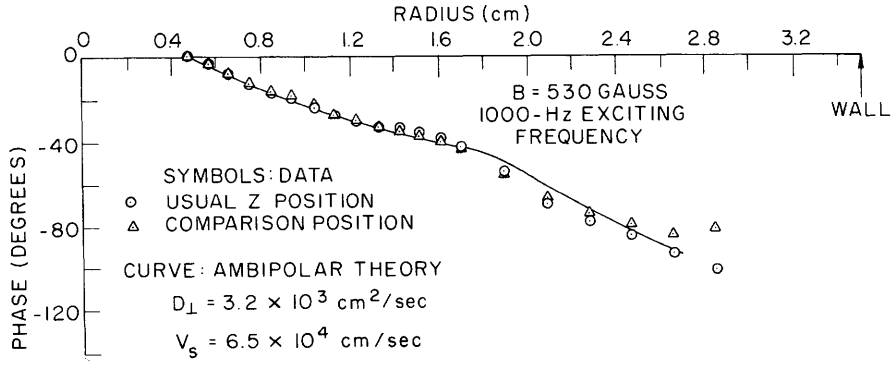

Fig. XXI-15. Diffusion-wave phase data from two longitudinal positions with theoretical curve.

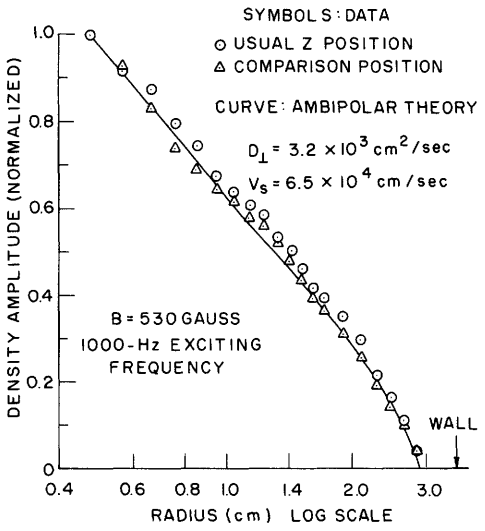

Fig. XXI-16. Diffusion-wave amplitude data from two longitudinal positions with theoretical curve.

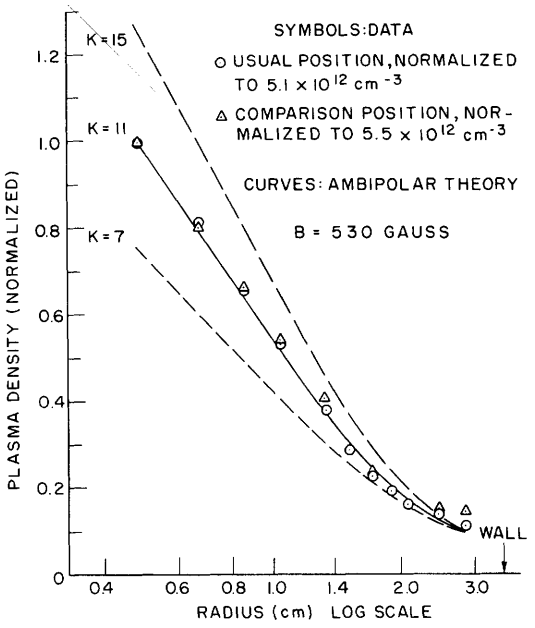

Fig. XXI-17. Plasma density at two longitudinal positions and theoretical curves.

propagation velocity of 1.3×10^5 cm/sec, away from the cathode. These data indicate that the assumption in question is reasonable.

5. Consistency of the Diffusion-Wave Results with the Steady-State Plasma

Figure XXI-17 also shows (smooth curve) a theoretical prediction of the plasma-density profile which is in agreement with the data. The curve was obtained by a computer solution of the nonlinear time-independent ambipolar diffusion equation, with the end-loss term and diffusion coefficient determined from the diffusion waves. The equation is

$$\frac{1}{R}\frac{\partial}{\partial R} R \frac{n}{T^{3/2}} \frac{\partial}{\partial R} nT = \kappa n T^{1/2},$$

where κ is a constant proportional to the ratio of (V_s/L) to $D_\perp$. The same approximation to the measured T_e profile was used as in the wave theory. A degree of fitting is possible because two boundary conditions are required to define a unique solution. The conditions were estimated from the data; specifically, $\partial n/\partial R = 0$ and $n = 10^{12}$ cm^{-3} at R = 2.85 cm.

Two other computer curves (dashed lines) show the effect of varying the constant κ away from the value determined from the diffusion-wave data. Thus the values obtained

from the diffusion-wave measurements are shown to be consistent with the static plasma density profile.

6. Results and Conclusions

The diffusion-wave technique has been successfully used to measure transverse diffusion coefficients in a dense highly ionized magnetically confined plasma. Ambipolar collisional diffusion theory provides the most satisfactory description of the experimental characteristics. The measured values of $D_\perp$ are in reasonable agreement with predicted values based on this theory, with the use of measured plasma parameters.

This relatively simple and accurate method of measuring diffusion coefficients would seem to be worthy of general consideration as a diagnostic technique in many steady-state plasma devices. A preliminary study indicates that the method should be feasible for such devices as the Q-machine, other hollow-cathode discharges, duoplasmation-generated plasmas, and some beam-generated plasmas.

D. L. Flannery

References

1. V. E. Golant, Soviet Phys. – Usp., p. 169, September-October 1963.
2. D. L. Flannery, Quarterly Progress Report No. 87, Research Laboratory of Electronics, M. I. T., October 15, 1967, pp. 64-71.

C. HELIUM AFTERGLOW DENSITY MEASUREMENTS UTILIZING A NARROW-BAND FAR INFRARED INTERFEROMETER

1. Introduction

A narrow-band far infrared interferometer has been constructed and employed to measure electron densities in the afterglow of a helium plasma. These measurements were made with the interferometer operating at an ~200-μ wavelength. The plasma is a repetitively pulsed cold-cathode discharge in a few Torr of helium with electron densities reaching 10^{14} cm^{-3}.

A complete description of the mechanics of the interferometer, together with a Kirchhoff diffraction solution of its optics for an infinitesimal frequency width, $\omega \rightarrow \omega + d\omega$, has been described previously.[1] In this report the actual method of phase-shift measurements will be demonstrated. Since the interferometer and detector accept a finite bandwidth from the Hg arc source, it is necessary to integrate the monochromatic Kirchhoff diffraction solution over the bandwidth. This problem will be dealt with here and the introduction of an adjustable beam length for one arm of the interferometer will be shown to allow rapid experimental measurements of the effective operating wavelength and bandwidth. Because of the energy limitations of the Hg arc source, the beam diameter

has to be sizable; thus the limitation on the maximum measurable phase shift resulting from plasma density gradients within the beam must be considered. Finally, the application of this interferometer to the measurement of the time dependence of electron densities in a helium afterglow, and comparison of this experiment with the theory for density decay in helium of Bates and Kingston[2] will be made.

2. Method of Experimental Phase-Shift Determination

The narrow-band interferometer is a two-beam instrument using lamellar diffraction gratings to split the radiation into a reference and sample beam and then recombine the two beams. As represented in Fig. XXI-18, symmetric angular positions of the two far

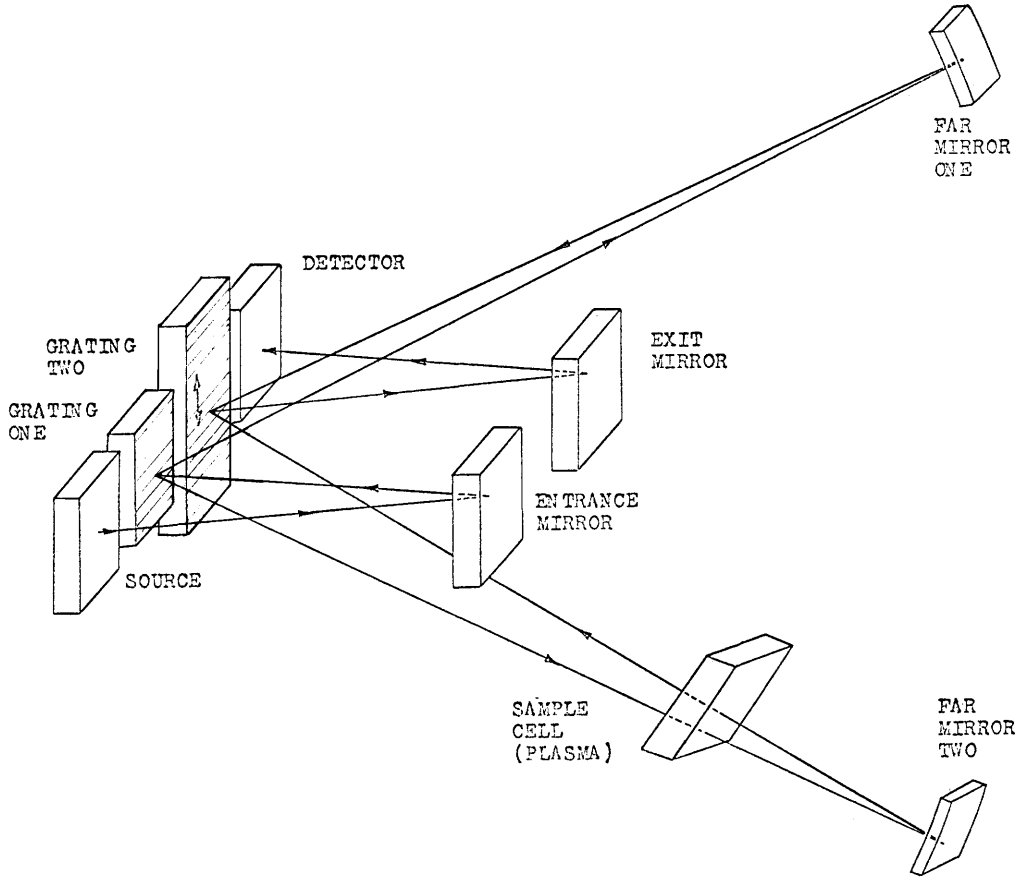

Fig. XXI-18. Block diagram of the interferometer optics.

mirrors about the normal to the gratings in a plane perpendicular to the grating surface defines the effective wavelength of operation. The gratings have a variable groove depth so that they may be tuned for maximum efficiency at a given wavelength.[3] As shown by the arrows in Fig. XXI-18, grating 2 may be moved relative to grating 1, this movement

being designated Δ. Because of the interference pattern produced by the two beams incident on grating 2, the output normal to grating 2, which is accepted by the detector, is dependent both on Δ and on the phase shift in the sample beam.

This important dependence, as demonstrated in the Kirchhoff diffraction solution for monochromatic radiation, is

$$I_D \sim \cos^2\left[2\pi\frac{\Delta}{d}+\Phi\right], \tag{1}$$

where I_D is the intensity incident on the detector, d is the grating groove spacing, and Φ is the phase shift attributable to the sample. Since grating 2 is twice the length of grating 1 (and therefore twice as big as the beam size defined by grating 1), it can be driven continuously across the beam, with Δ allowed to change, from one end to the other, by an amount Nd, where N is the number of grooves in grating 1. By varying Δ linearly with time, the output of the detector, recorded on a strip chart moving synchronously with Δ, is the sinusoidal modulation given by Eq. 1. Now, if the 3-μsec sampling gate pulse, which is synchronous with the repetitively pulsed plasma, is delayed to a time far out in the afterglow, Φ = 0, and Δ increases linearly with time, a reference modulation is recorded as shown on the left side of Fig. XXI-19. With the Δ movement

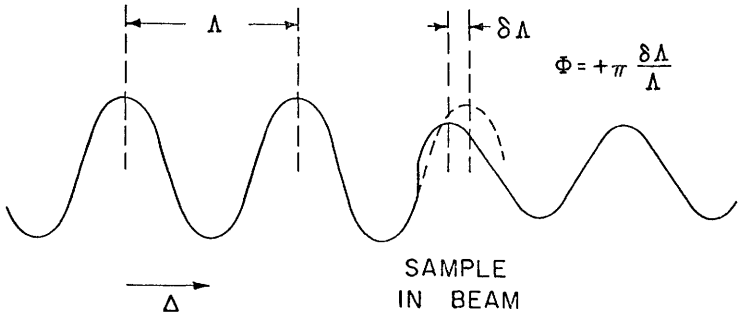

Fig. XXI-19. Modulation output of the interferometer.

uninterrupted, the sampling gate is set into the earlier afterglow, where Φ is measurable and the shift in the output modulation δΛ (shown in Fig. XXI-19) is immediately related to Φ. After a few modulations at this afterglow time, the gate can be reset for a new time, and thus Φ as a function of time in the afterglow is measured.

To determine δΛ and hence Φ, it is useful to construct a transparent template with a sinusoid of repetition length Λ engraved on it along with lines indicating the maxima and minima of this sinusoid. Since Λ depends only on d and the drive rates, the modulations are achromatic and the template works for all frequencies. Then it is a simple matter, purely by eye, to determine the position of the modulation maxima for each time,

and thus determine $\delta\Lambda$ with an accuracy of $\pm \frac{1}{20}\Lambda$. For plasmas with $\omega_p \equiv \left(\frac{n_e e^2}{\epsilon_o m}\right)^{1/2} \ll \omega$, the phase shift may be written

$$\Phi = 2.82 \times 10^{-17} \overline{n_e L} \cdot \lambda cm^2 \mu^{-1}, \tag{2}$$

where ω_p is the plasma frequency; ω, the infrared frequency; λ, the infrared wavelength; and $\overline{n_e L}$, the line density through which the beam passes. It follows that the sensitivity of the interferometer for line-density measurements is $\sim 6 \times 10^{15}\ \lambda^{-1}\ cm^{-2}\ \mu$. To determine the upper limits on measurable values of $\overline{n_e L}$, it is necessary to include bandwidth and beam-size considerations.

3. Finite Bandwidth Theory and Measurement

Although the period of the output modulation Λ is not frequency-dependent, the phase shift attributable to a plasma is, as Eq. 2 shows. Since the far mirrors accept a finite area of the diffraction pattern of grating 1, there is a finite bandwidth of frequencies passing through the interferometer. When Φ is zero or a constant independent of frequency, the interference patterns from the different frequencies formed on grating 2 by the two beams are identically positioned. If Φ is frequency-dependent, the positions of the patterns for different frequencies are shifted relative to each other, and the output modulations deteriorate.

From the discussion of partially coherent light by Born and Wolf,[4] the total intensity incident on the detector is given by integrating the square of the absolute value of the complex amplitude for the monochromatic solution over the frequency bandwidth

$$I_D = \frac{1}{\pi} \int_{\omega_1}^{\omega_2} F^2(\omega)\, U_D^*(\omega)\, U_D(\omega)\, d\omega. \tag{3}$$

The amplitude envelope $F(\omega)$ has been introduced to account for the output spectrum of the Hg arc source, water-vapor absorption, variations in detector sensitivity with frequency, and the lamellar grating efficiency. This leaves the square of the complex amplitudes equal to the modulation term, Eq. 1, except for some inessential constants. It is convenient to define new variables $\beta = \frac{\omega - \omega_o}{\omega_o}$, $\omega_o = \frac{\omega_2 + \omega_1}{2}$, and $\beta_o = \frac{\omega_2 - \omega_o}{\omega_o}$, so that $F^2(\omega)$ and $\Phi(\omega)$ may be expanded in Taylor series about ω_o,

$$F^2(\omega) \equiv \sum_{r=0}^{\infty} b_r \beta^r \tag{4}$$

and

$$\left[2\pi \frac{\Delta}{d} + \Phi(\omega)\right] \equiv \frac{1}{2} \sum_{s=0}^{\infty} c_s \beta^s. \tag{5}$$

This integration can now be carried out,[5] and the result is

$$I_D \sim \cos\left[4\pi \frac{\Delta}{d} + 2\Phi(\omega_o)\right]\left[b_o \cos c_1\beta_o + \frac{c_1 b_1}{2c_2}\left(\frac{\sin c_1\beta_o}{c_1\beta_o} - \cos c_1\beta_o\right)\right], \tag{6}$$

as long as

$$\left|c_2\beta_o^2\right| = \left|\left(\frac{d^2}{d\beta^2}\Phi(\beta)\right)_{\beta=0}\beta_o^2\right| \ll \left|4\pi \frac{\Delta}{d} + 2\Phi_{\beta=0}\right| \tag{7}$$

and

$$\left|c_3\beta_o^3\right| = \left|\left(\frac{d^3}{d\beta^3}\Phi(\beta)\right)_{\beta=0}\beta_o^3\right| \ll 1. \tag{8}$$

These conditions are very well satisfied when β_o is only a few per cent, and Φ is due to a plasma such that $c_o = -c_1 = c_2 = -c_3$. Thus the total intensity is proportional to the required modulation term times an envelope. The modulation envelope has a width at half-maximum of $\delta(c_1\beta_o) \approx \frac{2}{3}\pi$, so that for a plasma phase shift the largest change in phase shift that can be measured is

$$(\delta\Phi)_{max} = \frac{\pi}{3\beta_o}. \tag{9}$$

This limit has been stated in terms of a change in phase shift. If the interferometer is initially balanced before the plasma is introduced, then Φ_{max} is only one-half the value of $(\delta\Phi)_{max}$. For this reason, it is convenient to unbalance the interferometer and compensate one arm so that the full $\delta\Phi$ that is available can be used. A convenient method of accomplishing this is to make a far mirror movable, to lengthen or shorten one beam at will. In fact, if one is willing to recompensate the beam during the measurements, it is possible to shift the envelope a number of times and extend the limit by a factor of 10 to give

$$(\delta\Phi)_{\substack{max \\ comp}} \approx \frac{10\pi}{3\beta_o}. \tag{10}$$

The movable far mirror is useful also in measuring the wavelength of operation accurately and in obtaining an approximate value of the bandwidth. By having a micrometer drive to position the far mirror, measurements can be made of the phase shift as a function of far-mirror movement without the presence of a plasma. Since the phase

shift caused by the beam length is $\Phi_B = \frac{2\pi}{\lambda}\ell$, where ℓ is the length of the sample beam minus the reference beam, it follows that the slope of a plot of $\delta\Lambda$ against ℓ is $\frac{d\delta\Lambda}{d\ell} = \frac{2\Lambda}{\lambda}$. An example of this is shown in Fig. XXI-20, where the effective operating wavelength is

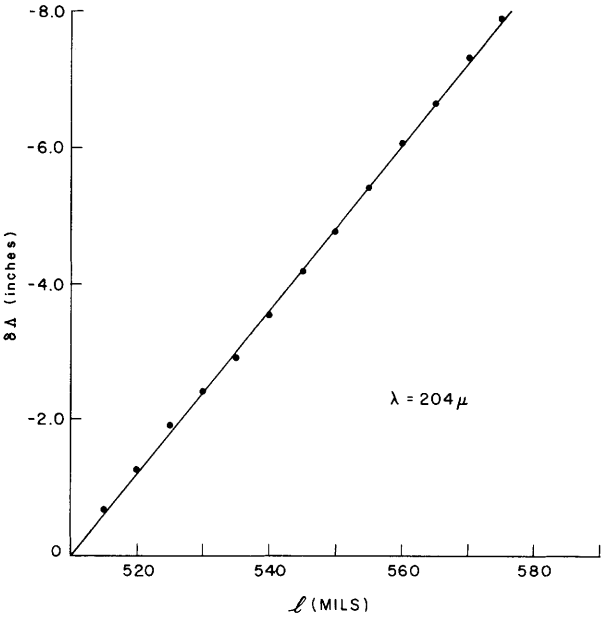

Fig. XXI-20. Measurement of the effective wavelength of operation.

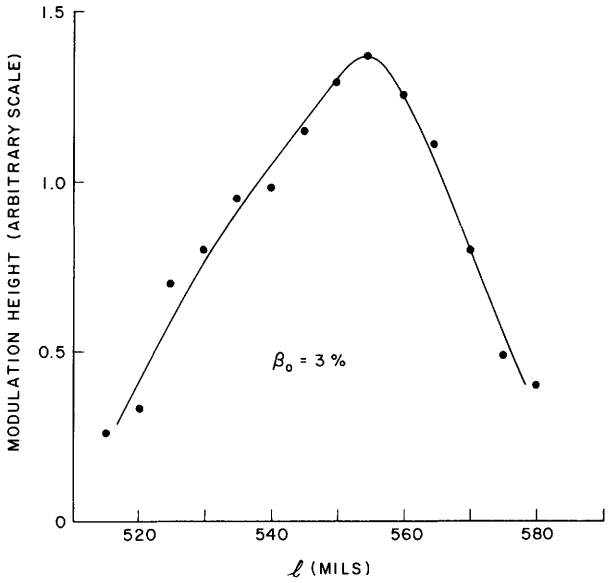

Fig. XXI-21. Effective bandwidth measurement.

determined to be 204 μ, with an accuracy better than 2%. A plot of modulation height against ℓ can be made from the same run, and the width of this measured envelope at half-maximum, $\delta\ell$, will give the bandwidth $\beta_o \approx \frac{\lambda}{6\delta\ell}$. In this case, as presented in Fig. XXI-21, $\beta_o \approx 3\%$. From these operational values and Eqs. 4 and 5, the maximum line densities that can be measured for a plasma without density gradients become

$$\overline{n_e L}_{max} \approx 3 \times 10^{15} \text{ cm}^{-2} \tag{11}$$

and

$$\overline{n_e L}_{\substack{max \\ comp}} \approx 3 \times 10^{16} \text{ cm}^{-2}. \tag{12}$$

4. Plasma Density Gradient Effects

For plasmas whose size transverse to the beam is somewhat larger than the interferometer beam size and with $\omega_p^2 \ll \omega^2$, the difference in phase shift resulting from refraction inside the plasma is negligible. Also, the effects of spatial dispersion are

not strong enough to give a significant loss in the sample beam. Thus it is possible to consider the rays traversing the plasma as traveling in undeviated straight lines. A problem that cannot be neglected, however, is that these rays see different line densities, determined by their position relative to the coincident axes of the beam and the plasma. Because the angles that rays make with the beam axis are quite small, they may be approximated as straight lines parallel to the beam axis. Since these rays will undergo different phase shifts, determined by their distance from the plasma axis, the output must be found by integrating over the beam. Therefore

$$I_D \sim 2\pi \int_0^{\rho_o} G(\rho) \cos^2 \left[2\pi \frac{\Delta}{d} + \Phi(\rho) \right] \rho \, d\rho, \tag{13}$$

where ρ_o is the maximum beam radius, $G(\rho)$ represents the intensity per unit area of the beam in the annulus between ρ and $\rho + d\rho$, and $\Phi(\rho) \equiv \frac{2\pi}{\lambda n_c} \overline{n_e L}(\rho)$. Here n_c is the critical density corresponding to a plasma frequency equal to the diagnostic frequency. By introducing the variable $y_m = \frac{\rho^2}{r_o^2} - \frac{\rho_o^2}{2r_o^2}$, where r_o is the radius of the plasma cross section, an integral equivalent to that in the previous section results. The solution of this integral again gives the modulation function times an envelope. To remain within the envelope, so that the modulations are measurable, requires

$$\left| \left(\frac{d\Phi(y_m)}{dy_m} \right)_{y_m=0} \cdot \frac{\rho_o^2}{r_o^2} \right| \lesssim \frac{\pi}{3}.$$

If the plasma tube used here is assumed to have a diffusion profile, where $r_o = 2$ inches, $L = 3$ inches, and $\rho_o = \sqrt{2}\,\frac{5}{8}$ inches, then the maximum measurable center density is $n_e \approx 3 \times 10^{14}$ cm^{-3}. This is a rather strict limitation, but it can be significantly relaxed by only a small decrease in ρ_o.

5. Plasma Measurements and Comparison with Theory

The plasma tube that was used is shown in Fig. XXI-22; it consisted of a cylindrical cold cathode whose inner surface was the emitter. Two circular Pyrex plates at either end of the cathode cylinder held the transparent grid anode, a smaller coaxial cylinder, in place. The centers of the Pyrex end plates were cut out and two crystal quartz plates were sealed on to allow the infrared beam to traverse the plasma along its axis. A continual flow of helium passed through the tube to keep the wall impurities from building up. With a 40-μsec, 1.5-kV pulse across the tube, a dense negative glow was produced which penetrated the anode and filled the core of the tube (4 inches in diameter, and 3 inches long).

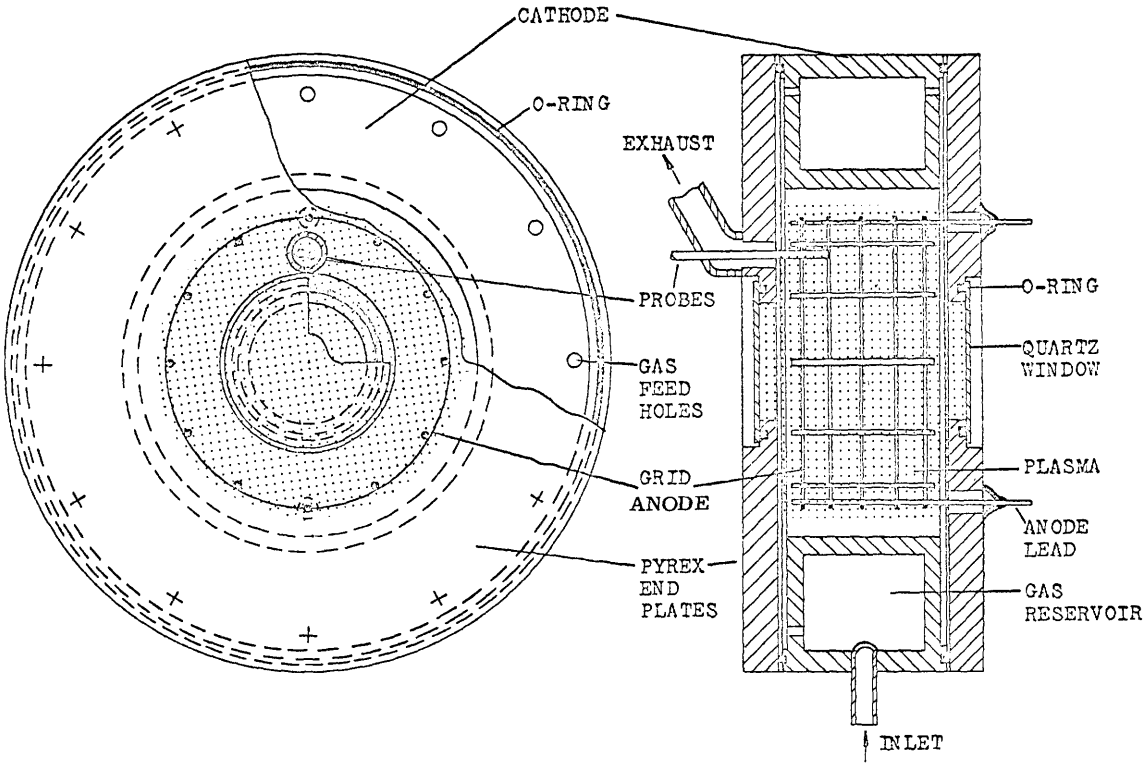

Fig. XXI-22. Diagram of the plasma tube.

Electron density measurements were made during the plasma excitation pulse and out to 200 μsec into the afterglow for plasma excitation pulses from 10 to 50 amps at 3 Torr and for pressures from 0.6 to 6 Torr at a current of 24 amps. Samples of these data are shown in Fig. XXI-23. Experimental decay times $\left(\frac{d \ln n_c}{dt}\right)^{-1}$ are of the order of 2×10^{-5} sec. Because of the short excitation pulses and the early afterglow times considered here, the maximum He_2^+ production rate previously published,[6] $\frac{\partial}{\partial t}\left(n_{He_2^+}\right) = 135\, p_o^2 n_{He^+}$ sec^{-1}, is too small to make an appreciable fraction of the ions into He_2^+. Therefore, dissociative recombination can be neglected. Also, the decay times for diffusion, impurity attachment, radiative recombination, and three-body recombination with neutrals all give decay times that are much too long.

Fortunately, a theory of collisional-radiative recombination for case (i) of optically thin and case (ii) of optically thick helium plasmas has been developed by Bates and Kingston,[2] which includes electron-electron-ion collisional recombination, together with radiative recombination and collisional or radiative de-excitation. Futhermore, since the electron temperature decay affects the rate of electron density decay, they have included energy losses in their theory. Thus inclusion of losses resulting from elastic collisions and charge exchange gives an expression for the electron density decay only

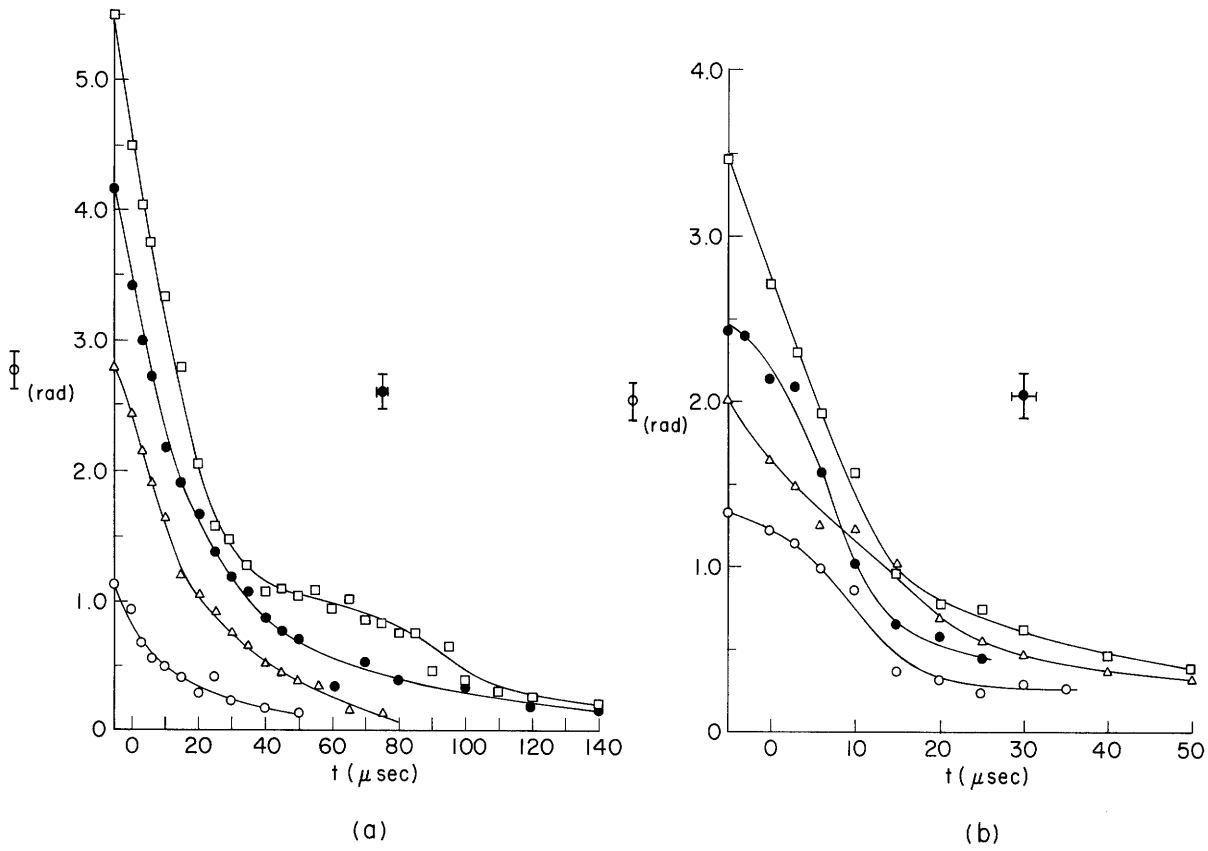

Fig. XXI-23. (a) Experimental data for plasma phase shift in the afterglow at 3 Torr. The symbols represent different plasma excitation currents: ○ 10 amps; △, 20 amps; × 30 amps; and □, 45 amps.

(b) Experimental data for plasma phase shift in the afterglow at various pressures. All data were taken with a plasma excitation pulse of 24 amps. The symbols represent different helium pressures: ○ 0.6 Torr; △, 2 Torr; □, 4 Torr, and × 6 Torr.

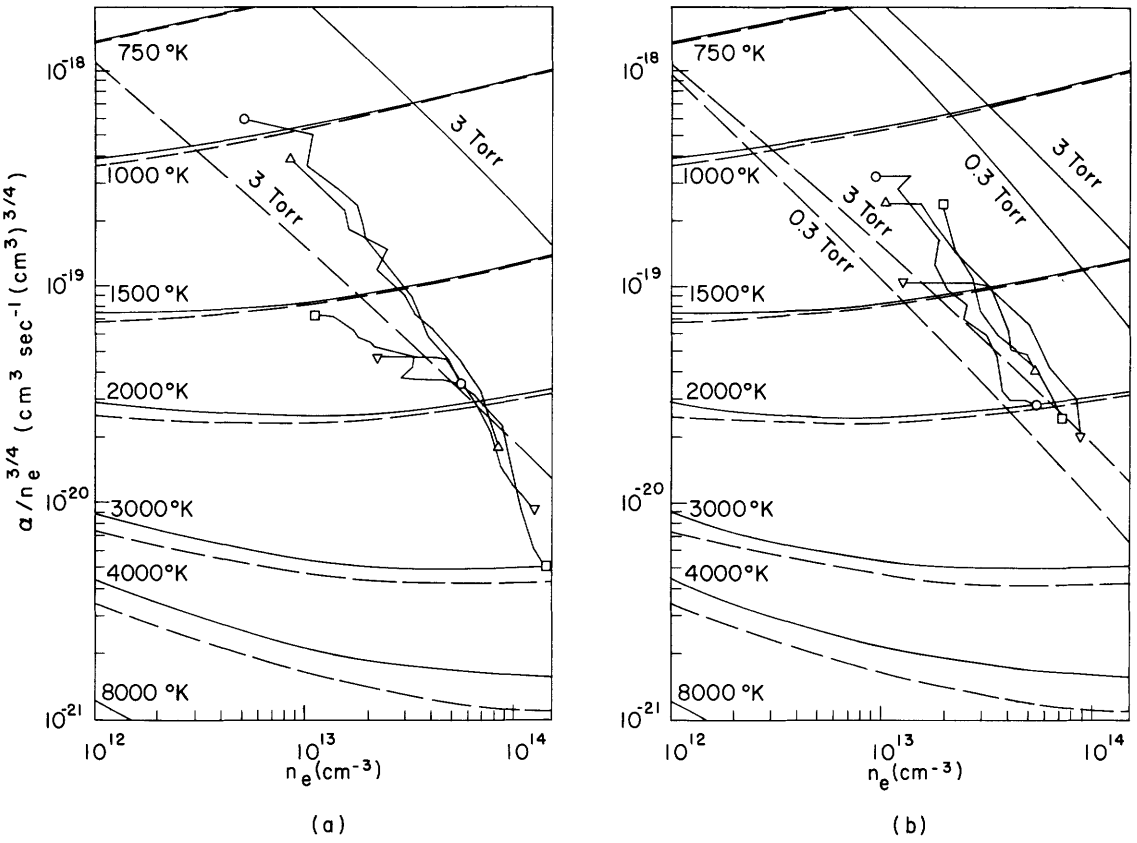

Fig. XXI-24. (a) Comparison of collisional-radiative decay theory with experiments in 3-Torr He. The smooth solid lines apply to the optically thin theory; and the dashed lines to the optically thick theory. The jagged lines are plots of the experimental data with straight lines drawn between points. The symbols refer to different plasma excitation currents: O, 15 amps; Δ, 25 amps; X, 35 amps; and □, 50 amps.

(b) Comparison of collisional-radiative decay theory with experiments at different pressures. The smooth solid lines apply to the optically thin theory, and the dashed lines to the optically thick theory. The jagged lines are plots of the experimental data with straight lines drawn between points. All data were taken with a plasma excitation pulse of 24 amps. The symbols refer to different pressures: O, 1 Torr; Δ , 2 Torr; X, 4 Torr; and □, 5 Torr.

in terms of initial neutral and electron densities and the optical thickness of the plasma. Thus, the theory can be compared directly with the measurements of the electron density decay without introducing the temperature as a separate parameter.

This theory may be compared with the interferometer measurements shown in Fig. XXI-24. Since the collisional-radiative recombination coefficient is approximately dependent on $n_e^{.75}$ in this density range, the coefficient has been divided by $n_e^{.75}$ to give a quantity nearly independent of density. The profile of the plasma is not well known, but is assumed to give a line density to center density ratio half-way between a pure diffusion profile and a pure recombination, uniform profile. Thus the experimental decay should give the correct slope on the plot of $\alpha/n_e^{.75}$, even though its position along the n_e axis is not determined with certainty to better than ±25%. It should be noted that in time-dependent computer solutions of the profile for two-body recombination afterglows[7] the profile does not change appreciably in times considered here of less than one-tenth of a diffusion time. We can determine $\alpha/n_e^{.75}$ experimentally by noting that $\frac{d}{dt}(n_e) = -\alpha n_e^2$ or $\frac{4}{7}\frac{d}{dt}\left(n_e^{-1.75}\right) = \alpha/n_e^{.75}$; hence, four-sevenths times the slope of a plot of $n_e^{-1.75}$ against t yields $\alpha/n_e^{.75}$.

Reasonable agreement in the early afterglow is obtained with the optically thick theory. Because the optically thick theory is developed to include large metastable populations and takes into account their rate of population change caused by radiation and electron collisions, it is not surprising that this is the appropriate case to consider. In the measurements for higher plasma excitation currents, there is a sudden deviation from the theory at ~30 μsec into the afterglow. This decrease in the rate of loss of electrons can be attributed actually to the production of electrons in the afterglow through metastable-metastable collisions. These proceed at a rate[8] of $\frac{\partial}{\partial t}(n_e) = 1.2 \times 10^{-9} (He^*)^2$ cm^3 sec^{-1}, and it is not unusual to find metastable populations in the early afterglow approaching the electron densities.[9] The theory is not designed to deal with this, since no atom-atom de-excitation collisions are taken into account.

M. L. Andrews

References

1. M. L. Andrews, Quarterly Progress Report No. 85, Research Laboratory of Electronics, M. I. T., April 15, 1967, pp. 87-97.

2. D. R. Bates and A. E. Kingston, Proc. Roy. Soc. (London) A279, 32 (1964).

3. M. L. Andrews, Quarterly Progress Report No. 74, Research Laboratory of Electronics, M. I. T., July 15, 1964, pp. 74-78.

4. M. Born and E. Wolf, Principles of Optics (Pergamon Press, London, 3rd edition, 1964), pp. 494-499.

5. M. L. Andrews, Ph. D. Thesis, Department of Physics, M. I. T., 1967.
6. E. C. Beaty and P. L. Paterson, Phys. Rev. 137, A346 (1965).
7. E. P. Gray and D. E. Kerr, Ann. Phys. 17, 276 (1959).
8. A. V. Phelps and J. P. Molnar, Phys. Rev. 89, 1202 (1953).
9. E. R. Mosburg, Phys. Rev. 152, 166 (1966).

D. ION TEMPERATURE MEASUREMENTS IN THE HOLLOW-CATHODE ARC PLASMA

1. Introduction

This report describes some measurements of the temperature of ions in the hollow-cathode arc plasma. A pressure-swept Fabry-Perot interferometer is used to determine the Doppler breadth of an emission line radiated by plasma ions. An objective of this project is the measurement of the radial variation of ion temperature. The preliminary results presented here indicate an apparent increase of ion temperature with radial coordinate. This appearance suggests that the plasma is undergoing azimuthal motion, for example, rotation. The optical system accepts light from a range of radii in the plasma, and the corresponding range of Doppler shifts arising from radially varying azimuthal motion would have the same effect as an increase in the Doppler breadth of the line.

2. Apparatus

The pressure-scanned Fabry-Perot apparatus is patterned on the design of Biondi.[1] The interferometer itself employs a 0.5-cm spacer like that described by Phelps[2] and $\lambda/50$ plates, 2 inches in diameter, with broadband dielectric coatings. The computed finesse and resolving power are 19.2 and 3.5×10^5 (at 5000 Å), respectively.

The hollow-cathode plasma[3] is viewed through a flat window in the front of a Pyrex section equipped with a flat sloping rear surface to minimize the reflection of light from the center of the plasma. The light is collected by a lens at its focal length from the center of the plasma. An interference filter with 5 Å bandwidth selects a singe emission line for the interferometer. The filter can be rotated to select the wavelength of the line. The argon lines at 4658 Å, 4610 Å, and 4545 Å and the neutral lines at 4642 Å and 4596 Å can be selected. The Fabry-Perot interferometer is mounted in a pressure can equipped with input and output windows and couplings that enable the operator to adjust the parallelism of the interferometer plates without opening the can. To make this adjustment, the fringes are observed visually through the output window. In operation the can is evacuated and argon gas is allowed to leak in slowly from a tank with a regulator set at a high pressure (21 psig) so that the pressure in the can changes very

nearly linearly with time while the first two fringes are scanned.

A lens outside the pressure can focuses the transmitted fringe pattern on a screen that has a pinhole, 0.010 inch in diameter. The lens-to-screen distance can be adjusted by an external screw that slides the lens along the axis. A spring-loaded micrometer adjustment permits centering the pinhole on the fringe pattern. This adjustment is made by replacing the pinhole with crosshairs and centering the cross on the pattern visually.

The liquid-air-cooled photomultiplier mounting is similar to one described by Bronco, St. John, and Fowler.[4] The output of the RCA 7850 photomultiplier is displayed on an X-Y recorder, with the x-axis time swept to yield a direct record of intensity as a function of wavelength.

The optical system, including the lenses, interferometer, and detector are mounted on an optical bench that can be raised and lowered with respect to the plasma by three screws.

3. Data Analysis

The apparent breadth of a line recorded by the scanning interferometer is greater that the thermal Doppler breadth, because of instrument broadening and Zeeman splitting of the emission line.

The instrumental broadening is measured by scanning the profile of the 6334 Å line emitted from a neon glow lamp. The relation connecting the true width, instrument width, and the observed width, obtained by the convolution of the Doppler and Airy profiles, has been presented in tabular form by Krebs and Sauer,[6] and graphically by Tako and Ohi.[7] The results of these calculations are used to determine the magnitude of the instrument breadth from the observed breadth of the neon line, under the assumption that the true width is its Doppler width at 300 K (0.0434 cm^{-1}). It should be noted that the Airy formula is derived under the assumption that the interferometer plates are perfectly flat and parallel. Hence the application of the calculations[6,7] to a real instrument is an approximation. Experimental evidence suggests that the error in the half-width resulting from the approximation is not too large when the parallelism of the plates is in good adjustment. The measured instrumental width when the interferometer is well adjusted is 0.055 cm^{-1} which compares fairly well with the value 0.0523 cm^{-1} computed from the reflection coefficient and the surface figure of the plates.

The true breadth of a line scanned in measurements on the arc plasma is obtained from the observed width by inverting the calibration process to obtain the true width from the measured width and the known instrument breadth.

The effect of Zeeman splitting on the observed line profile can be essentially removed by inserting a polarizing filter with its axis parallel to the magnetic field so that only the Zeeman π components reach the interferometer.[5] The π components are shifted very little from the zero field wavelength of the line (less than or of the order

of 10^{-3} Å at fields up to 1000 Gauss for the lines observed in these experiments). The apparent increase in the breadth of a line, because of this splitting, is small compared with its thermal breadth.

4. Results

The experimental results are shown in Fig. XXI-25 where the ion temperature and the intensity of the observed ion line are given as a function of the vertical position of

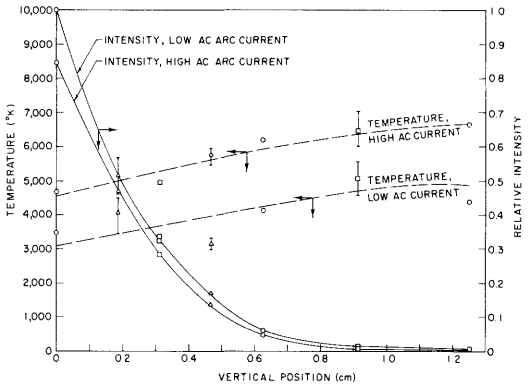

Fig. XXI-25. Experimental results.
⊙ Data of 11/28/67.
⊡ Data of 11/29/67.
△ Data of 12/4/67.

the interferometer. At zero vertical position the axis of the optical system passes through the center of the plasma. The line observed for these measurements was the 4658 Å line of A II. The arc current was 10 amps, the flow rate was 70 atm-cc/min and the axial magnetic field was 600 Gauss. Two sets of measurements were made: one when the AC arc current was high (~70 mA) and one when the AC arc current was low (~7 mA). The AC arc current is taken as a measure of the amplitude of the noise in the plasma. The noise level is controlled by adjusting the position of one of the gate valves. This means that the pressure is lower (4.5 μ) in the high-noise case and higher (8 μ) in the low-noise case. (The quoted pressures were measured near the anode; in the cathode region the pressure was roughly the same in the two cases, 1-2 μ.) The error brackets on some of the points represent the difference between the instrument breadth measured before and after the arc temperature measurement. For the points with no brackets, there was no change. The data taken on different days give an indication of the reproducibility of the results.

The magnitude of the ion temperature is approximately one-third to two-thirds of a volt.

The ion temperature remains high when the axis of the optical system is so far from the center of the plasma that the measured light intensity has dropped to less than 1% of its maximum value. There is, in fact, an apparent increase in the temperature with increasing vertical displacement which corresponds to line breadth increasing with

radial coordinate. This appearance may be due to azimuthal plasma motion, for example, rotation. The optical system accepts light from a range of radii and hence samples a range of velocities, if the plasma has radially varying azimuthal motion. The corresponding range of Doppler shifts would constitute a nonthermal Doppler broadening. rotating instabilities have been observed in the hollow cathode arc plasma,[8] but the data indicate that the present effect is not noticeably stronger in a noisy plasma than when the plasma is quiet. The E × B drift in the plasma is azimuthal and of the same order of magnitude as the ion thermal velocity. We plan to explore this effect further experimentally by attempting to determine if there is a shift in the center frequency of the line.

J. K. Silk

References

1. M. A. Biondi, Rev. Sci. Instr. 27, 36 (1956).
2. F. M. Phelps III, Opt. Soc. Am. 55, 293 (1965).
3. L. M. Lidsky, S. D. Rothleder, D. J. Rose, and S. Yoshikawa, J. Appl. Phys. 33, 2490 (1962).
4. C. J. Bronco, R. M. St. John, and R. G. Fowler, Rev. Sci. Instr. 29, 1145 (1958).
5. A. Eberhagen, M. J. Bernstein, and H. Hermansdorfer, Z. Naturforsch. 20a, 1375 (1965).
6. K. Krebs and A. Sauer, Ann. Physik 13, 359 (1953).
7. Toshiharu Tako and Misao Ohi, Jap. J. Appl. Phys. 4, Suppl. 1, 451 (1965).
8. D. L. Morse, Phys. Fluids 8, 516 (1965).